nature communications

Article

https://doi.org/10.1038/s41467-025-57820-8

Manipulations of a transmon qubit with a null-biased electro-optic fiber link

Received: 19 July 2024

Accepted: 27 February 2025

Wenqu Xu[1,2,3,5], Tingting Guo[1,2,3,5], Kaixuan Zhang[1,2,3], Zishuo Li[1,2,3], Tianshi Zhou[1,2,3], Quan Zuo[1,2,3], Yifan Sheng[1,2,3], Lingxiao Jing[1,2,3], Huashi Ma[1,2,3], Mingyuan Yu[1,2,3], Shunhong Zhou[1,2,3], Binglin Li[1,2,3], Shiyao Yang[1,2,3], Yongyang Yu[1,2,3], Junzhou Zhang[1,2,3], Jiyuan Zhu[1,2,3], Chunhai Cao[1,3], Guanghao Zhu[1,3] ✉, Guozhu Sun[1,2,3,4] ✉ & Peiheng Wu[1,2,3]

In recent years, significant progress has been made in the field of superconducting quantum circuits, particularly in improving the complexity of quantum processors for large-scale quantum computing and quantum simulation tasks. To enable the execution of quantum information processing tasks on large-scale quantum circuits containing millions of qubits, it is essential to minimize thermal effects on control and measurement lines, ensuring that circuit components are superconducting and that qubits are not significantly thermally excited. Recent studies have shown that a quadrature-biased electro-optic fiber link can operate qubits with a much reduced thermal load, thereby facilitating the simultaneous operation of a large number of qubits. Expanding on this, here we propose and demonstrate that coherent manipulations of superconducting qubits can also be achieved by setting the bias point of the electro-optic modulator at the null point instead of the quadrature point. Major advantages of our null-point bias method include further reduction of the thermal load and improvement of the signal-to-noise ratio, and relaxed requirement for experimental implementations. Simultaneous control of two qubits is also demonstrated using the proposed null-biased fiber-optic link, which is the first time to the best of our knowledge.

Over the past two decades, the scientific community has observed a notable surge in interest in superconducting quantum circuits[1–5]. Utilizing advanced chip design and manufacturing technologies, various types of novel superconducting qubits have been demonstrated. For example, with a large capacitor shunted to the small Josephson junction (or SQUID) or additionally introduced large Josephson junctions as inductors[6–8], qubit devices implemented by the transmon[9], the Xmon[10], the capacitively shunted flux qubit[11,12] and the capacitively shunted fluxonium[13] platform have been reported. These novel types of superconducting qubits are marked by their outstanding performance characterized by enhanced coherence[14–16], flexible controllability, and stable qubit coupling[17–20]. These advancements have effectively met the critical prerequisites for achieving large-scale quantum computing[5,21,22]. On the other hand, however, practical realization of universal quantum computation requires the simultaneous operation of millions of qubits at stable millikelvin temperatures[23–27], which is essential to sustain devices in a superconducting state and ensure the minimal thermal qubit excitations[28–32]. This thus presents a serious challenge for the thermal management of dilution refrigerators at stable millikelvin temperatures.

Recent studies have highlighted the potential of analog fiber-optic links[33,34], which are made of off-the-shelf devices in fiber-optic

---

[1]Research Institute of Superconductor Electronics, School of Electronic Science and Engineering, Nanjing University, Nanjing, China. [2]Purple Mountain Laboratories, Nanjing, China. [3]Hefei National Laboratory, Hefei, China. [4]Shishan Laboratory, Suzhou Campus of Nanjing University, Suzhou, China. [5]These authors contributed equally: Wenqu Xu, Tingting Guo. ✉e-mail: ghzhu@nju.edu.cn; gzsun@nju.edu.cn

communication community, to achieve control and measurement of highly coherent quantum states with performance comparable to those attained using traditional coaxial cable links[35–37]. The underlying principle involves up-converting microwave signals to optical signals using quadrature-biased electro-optic modulators (EOM), transmitting them through an optical fiber to cryogenic environment of millikelvin level, and down-converting them back to microwave signals using a photodiode to drive the qubit chips[34,35]. We note that this method offers an important advantage over microwave coaxial cable links in terms of thermal management because the thermal conductivity of optical fibers is nearly-zero[38]. Taking further account of the large intrinsic bandwidth of optical fibers, direct transmission of millions of signals to the millikelvin-level stages with much reduced passive thermal loads is thus possible. Consequently, this approach holds promise for the realization of large-scale superconducting quantum circuits. In parallel to these advancements, several schemes have been proposed and implemented for high-fidelity readout of superconducting qubits using acousto-optic modulators (AOM) and electro-optic modulators (EOM)[39–41]. These studies further highlight the potential of photonic techniques to enable the operation of large-scale quantum processors.

Building upon this foundation, here we propose and validate an alternative fiber-optic link approach for qubit control by biasing the EOM at the null point. As a validation, it is demonstrated that vector control of qubits can be achieved using the proposed null-biased fiber-optic link with performance comparable to that of the conventional microwave coaxial cable link, in terms of frequency domain distribution, amplitude range, and phase variation. Moreover, we also demonstrate parallel vector driving of two qubits, with an aim to show its potential application in large-scale quantum circuit manipulation tasks. We conduct numerical analyses to compare two linear modulation schemes using a quadrature-biased EOM with a nonlinear modulation scheme using a null-biased EOM. Our results indicate that the proposed null-biased approach offers significant advantages by simplifying the experimental setup and reducing RF instrumentation requirements. It is shown theoretically that the proposed null-biased technique offers improvements over the quadrature-biased technique in terms of maximum number of addressable qubits and signal-to-noise ratio (SNR), for a wide range of optical modulation depths and qubit driving duty cycle.

Results

Experimental setup

Similar to the first demonstration of the fiber-optic link-based control of qubits[35], the key component involved is an EOM (Mach-Zehnder intensity modulator), as depicted in Fig. 1. Note that owing to various

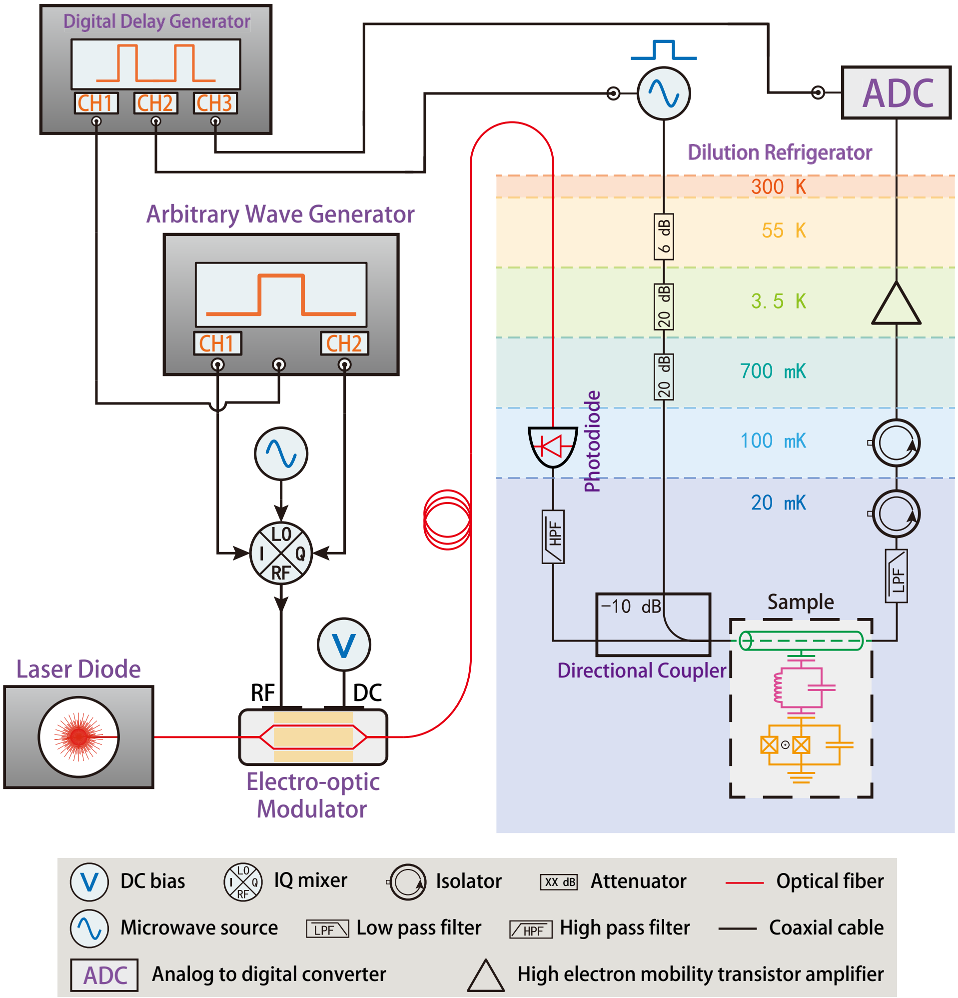

Fig. 1 | Schematics of the experiment setup for null-biased fiber-optic control of the qubit state. At the room temperature, the vector microwave signal generated by IQ mixing serves as the modulation voltage for the EOM. The modulated optical signal is then transmitted through an optical fiber (red line) to the cryogenic environment. Upon reaching the low temperature, a photodetector converts it to a microwave signal which is used to drive the qubit. In the dashed box, the green part is the coplanar waveguide transmission line, the pink part is a resonator and the yellow part is a transmon qubit.

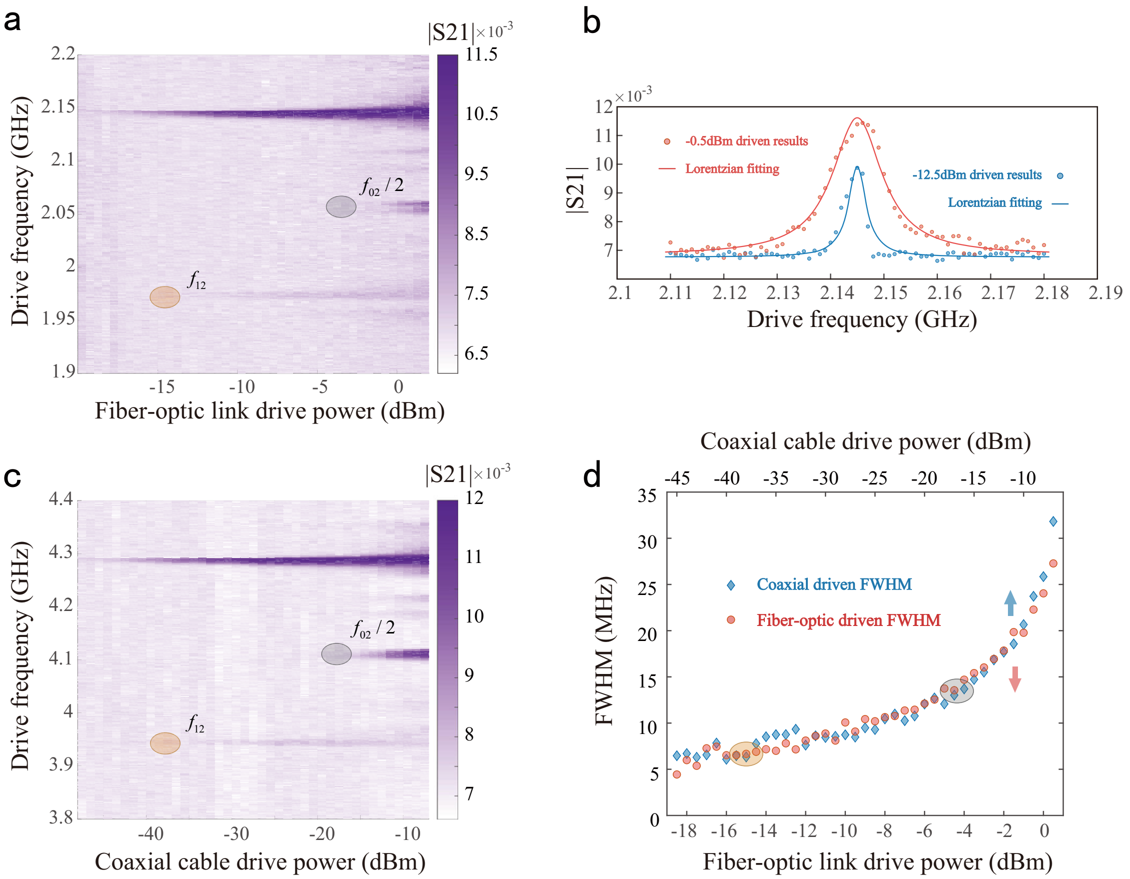

Fig. 2 | Two-tone spectroscopy versus the driving power. a Two-tone spectroscopy versus the driving poqer using the null-biased fiber-optic link. **b** Lorentzian fittings of the 0–1 transition frequency. **c** Two-tone spectroscopy versus the driving poqer using the coaxial cable link. **d** The linewidths of spectral peaks represented by the full width at half maxima (FWHM) at different power are extracted by performing the Lorentzian fittings. The orange and gray elliptical shading regions indicate the positions where the 1–2 and 0–2 (two-photon) transitions occur.

advantages outlined in the discussion section, here the EOM is biased at the null point instead of the quadrature point. Because of the null-biased nature of the Mach-Zehnder EOM, it follows that the frequency of the modulated optical signal is twice that of the modulator's microwave driving signal. This suggests that in order to resonantly control the qubit system, the EOM's modulation frequency needs to be half of the qubit frequency.

To validate the qubit control capability of the null-biased fiber-optic link, a transmon qubit is fabricated and tested using the setup depicted in Fig. 1. Specifically, the transmon qubit is capacitively coupled to a coplanar resonator[9,42], which is coupled to a transmission line. The input end of the transmission line is connected to a microwave coupler for controlling the state of qubits and probing the resonator for readout. The output end of the transmission line is connected to the room-temperature electronic equipment via microwave coaxial cables for signal acquisition and demodulation. In the room- temperature circuitry of the experimental system, two output channels of an arbitrary waveform generator (AWG) serve as the IQ inputs for the IQ mixer, which generates a vector signal to drive the EOM. The intensity-modulated optical signal after the EOM is transmitted via an optical fiber to the cryogenic refrigerator. On top of the mixing chamber plate inside the dilution refrigerator, the optical signal is converted back to microwave signal by a photodiode. This microwave signal (for qubit control) is combined with another microwave signal (generated by a separate microwave synthesizer for qubit readout) through a directional coupler, and transmitted to the input port of the sample.

Frequency domain characterization

We first characterize the qubit in the frequency domain. Figure 2a shows the two-tone spectroscopy result obtained with the qubit being driven by a null-biased fiber-optic link. As a comparison, Fig. 2c shows the same result obtained with the qubit being driven by a coaxial cable link. It can be seen that when the driving power is high enough, both results demonstrate similar behaviors, i.e., qubit transitions and photon number splitting, indicating that the proposed null-biased fiber-optic link is effective for qubit driving. For a more quantitative comparison, the linewidths of spectral peaks represented by the full width at half maxima (FWHM) at different powers[43] are extracted and fitted using the Lorentzian function as shown in Fig. 2b. For both driving methods, the linewidths of the 0–1 transition signals are nearly identical if the driving power falls into a certain range, as shown in Fig. 2d. In this range, the EOM's driving powers are from −20 dBm to −2 dBm for the case of null-biased fiber-optic link and from −46 dBm to −12 dBm for the case of coaxial cable link, respectively. Note that the shading areas in Fig. 2a and c indicate the positions of qubit transitions, which are used in Fig. 2d for the axis alignment of the EOM's driving power between the two cases. These obtained results confirm that when the field strength interacting with the qubit is the same, the power spectral densities of the continuous driving field generated by both methods, including both signal and noise components, remain essentially consistent. In other words, the null-biased fiber-optic link does not induce additional higher energy level excitations or cause extra decoherence effects.

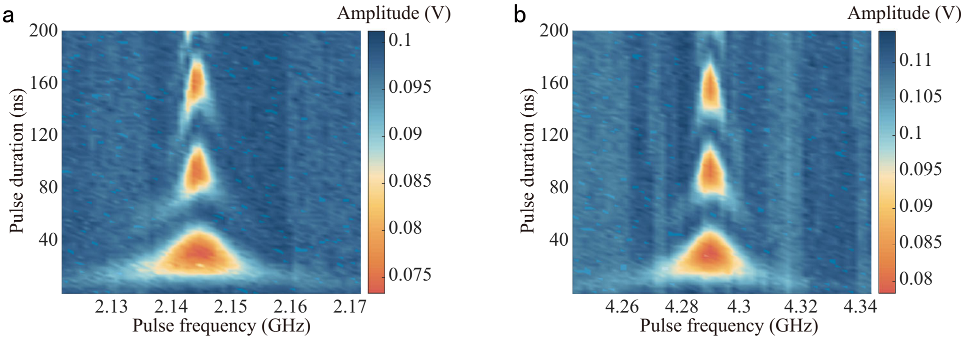

Fig. 3 | Rabi chevron patterns of the qubit. a The Rabi chevron pattern of the qubit driven by the null-biased fiber-optic link. **b** The Rabi chevron pattern of the qubit driven by the coaxial cable link. At the resonantly driving point, both links exhibit a Rabi frequency of approximate 16 MHz.

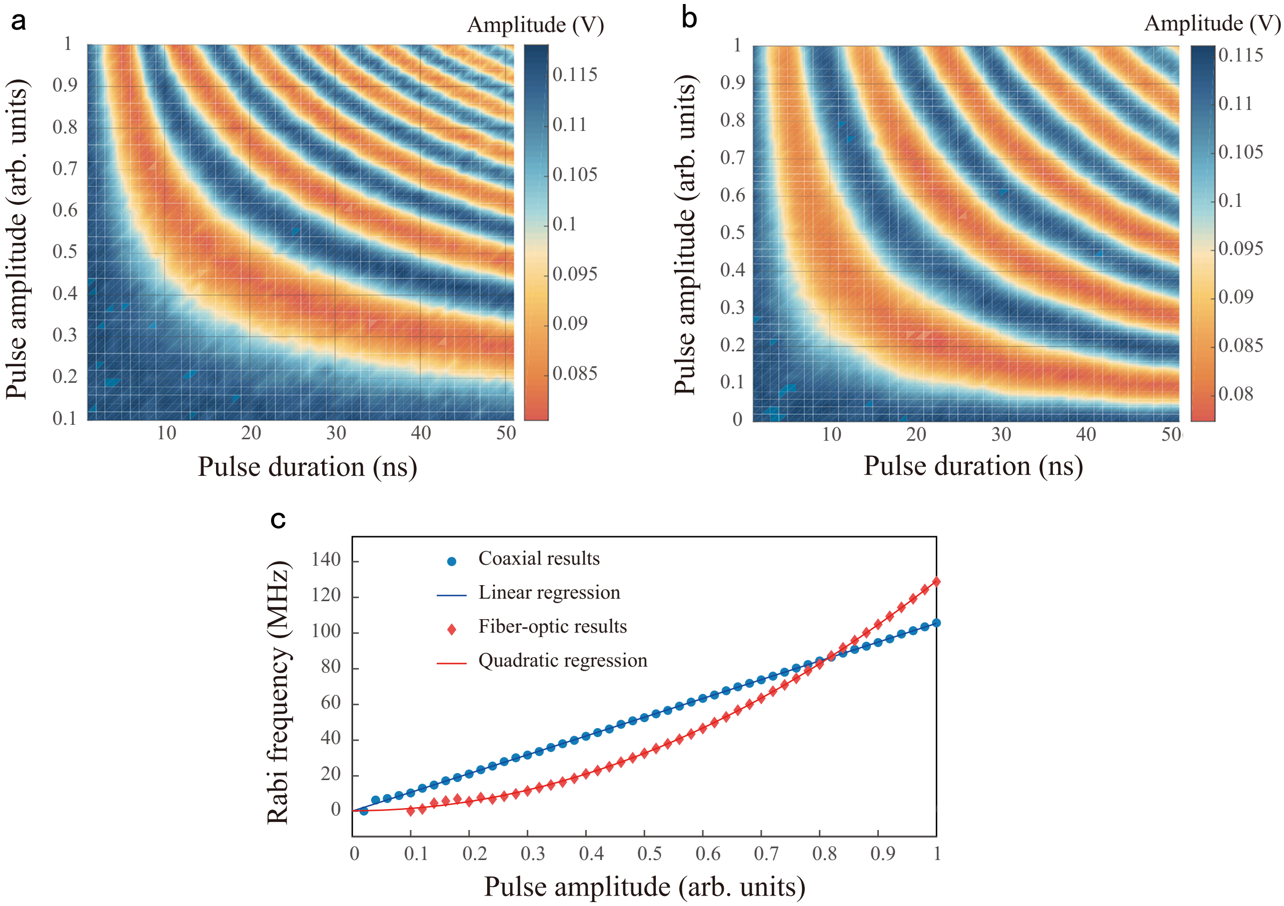

Fig. 4 | Rabi oscillations. a Rabi oscillation driven by the null-biased fiber-optic link with different amplitudes, showing a range of Rabi frequencies up to about 129 MHz. **b** Rabi oscillation driven by the coaxial cable link with different amplitudes, showing a range of Rabi frequencies up to about 106 MHz. **c** The extracted Rabi frequencies are fitted with linear and quadratic functions with respect to the amplitude of AWG driving signal, respectively.

Time domain characterization

Next, we characterize the qubit in the time domain. Figure 3a shows the measured Rabi chevron pattern when the qubit is driven by the null-biased fiber-optic link. As a comparison, Fig. 3b shows the same result obtained when the qubit is driven by a coaxial cable link. Note that when obtaining these results, square-wave pulses are used because such pulses possess the same temporal width before and after the up/down conversions of the null-biased fiber-optic link. As a result, one does not need to rescale the pulse-width axis of the Rabi chevron pattern of Fig. 3a. Moreover, for a justified comparison, the power of AWG sources is calibrated so that in both cases of the fiber-optic and coaxial cable links, the delivered square-wave pulses at the qubit end have the same amplitude. Note that in other characterizations, Gaussian shaped pulses have been used. Under these conditions, Fig. 3 shows that the obtained Rabi chevron patterns for both cases are nearly identical, except that in Fig. 3a, the frequency-axis ranges from 2.13 GHz to 2.16 GHz while in Fig. 3b the frequency-axis ranges from 4.26 GHz to 4.32 GHz. As mentioned before, such a difference of a factor of 2 is expected, since in the null-biased fiber-optic link the EOM's modulation frequency needs to be half of the qubit frequency (see the detail in Supplementary Note 1).

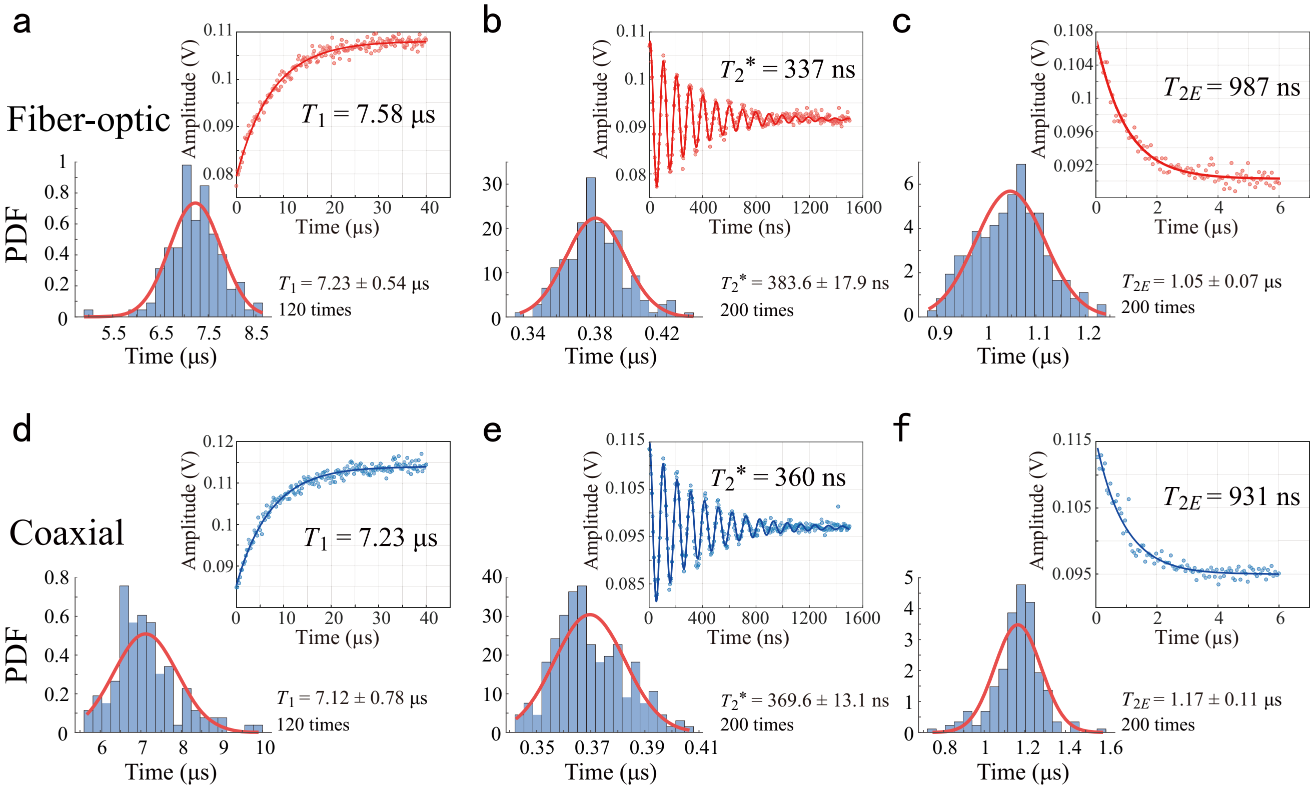

Fig. 5 | Statistical analyses of T_1, T_2^* and T_{2E}. a The histogram of 120 measurements for T_1 along with the typical experimental data and the corresponding fitting result (the inset) for the null-biased fiber-optic link. **b** The histogram of 200 measurements for T_2^* along with the typical experimental data and the corresponding fitting result (the inset) for the null-biased fiber-optic link. **c** The histogram of 200 measurements for T_{2E} along with the typical experimental data and the corresponding fitting result (the inset) for the null-biased fiber-optic link. **d** The histogram of 120 measurements for T_1 along with the typical experimental data and the corresponding fitting result (the inset) for the coaxial cable link. **e** The histogram of 200 measurements for T_2^* along with the typical experimental data and the corresponding fitting result (the inset) for the coaxial cable link. **f** The histogram of 200 measurements for T_{2E} along with the typical experimental data and the corresponding fitting result (the inset) for the coaxial cable link.

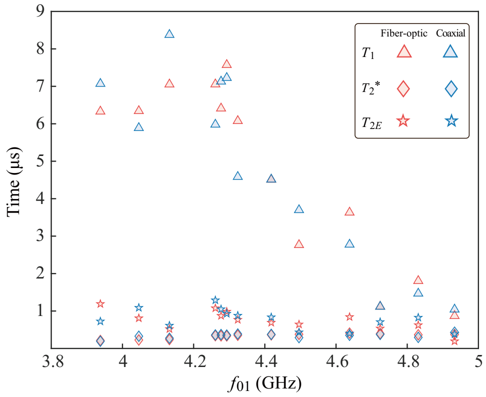

Fig. 6 | T_1, T_2^* and T_{2E} versus f_{01}. Measurements of T_1, T_2^* and T_{2E} versus f_{01} of the qubit driven by the two methods.

Then we vary the pulse amplitude to extract the Rabi frequencies. As shown in Fig. 4a and c, the Rabi oscillation frequency driven by the null-biased fiber-optic link exhibits a quadratic dependence on the AWG modulation amplitude, which is a result of the frequency doubling effect of the null-biased fiber-optic link. It is found that the highest Rabi frequency exceeds 100 MHz, indicating that the null-biased fiber-optic link meets the requirement for rapid quantum gate operations. As shown in Fig. 4b, we compare the results to those obtained via the coaxial cable link, where the Rabi frequency shows a linear relation to the driving amplitude of AWG. Furthermore, compared to the case of linear coaxial cable link, the quadratic relationship between the Rabi frequency and the driving amplitude suggests that a better on-off ratio for the output pulse signal may be achieved.

To determine the qubit decoherence performances, T_1, T_2^*, and T_{2E} for cases of null-biased fiber-optic link and coaxial cable link are measured. The results are shown in Fig. 5a–c and d–f, respectively. To provide further information, long-term statistical measurements of T_1, T_2^*, and T_{2E}, fitted with Gaussian distributions, are presented by Fig. 5. Here the flux bias point of the qubit is set to be $-0.35\,\Phi_0$, and 120 measurements of T_1, 200 measurements of T_2^*, and 200 measurements of T_{2E} are conducted along with Gaussian distribution fitting of the probability density function. The variations of qubit frequencies f_{01} ($=\omega_q/2\pi$) are achieved by changing the magnetic flux bias as shown in Fig. 6. Although the coherence time is limited to the possible magnetic noise and defects in the sample, it can be seen from Figs. 5 and 6 that the null-biased fiber-optic link and the coaxial cable link yield similar statistical results, leading to a conclusion that the null-biased fiber-optic link does not affect the decoherence performance of the qubit within the sensitivity limits posed by the coherence of the herein used qubits.

Vector control and parallelism

In the following part of this section, we demonstrate that the null-biased fiber-optic link can perform complete qubit manipulations of the Bloch vectors. To generate the signal that rotates the Bloch

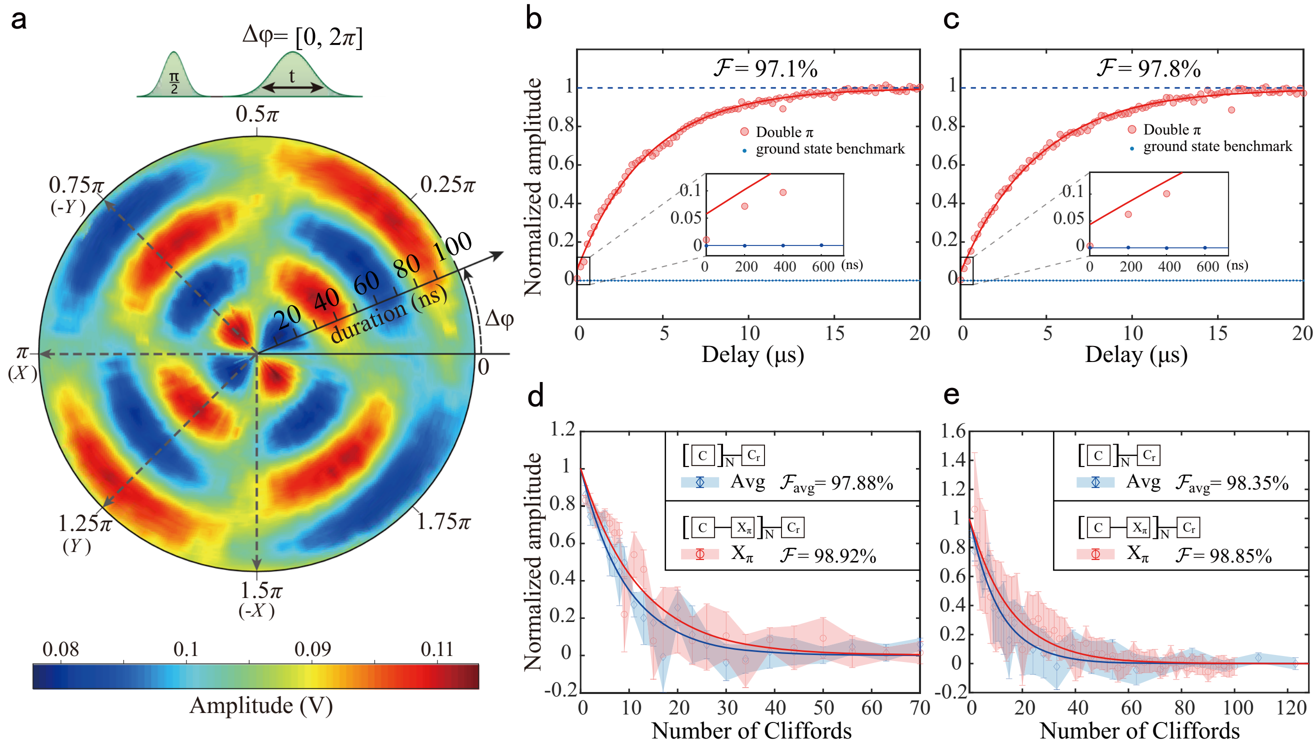

Fig. 7 | Tomography and gate fidelity. a Two-dimensional Rabi oscillation data in the polar coordinate. The qubit is initially prepared in the state $(|0\rangle + \mathrm{i}|1\rangle)/\sqrt{2}$ by sending the first pulse to rotate the Bloch vector $\pi/2$ around the X-axis. Then, we change the phase of the second pulse within the range of 0 to 2π and measure the population versus the pulse duration from 0 to 100 ns. The black dashed lines indicate the -Y, X, Y, and -X axes, with corresponding phase of 0.75π, π, 1.25π and 1.5π for the second pulses, respectively. **b** The fidelity of the π pulse driven by the coaxial cable link is 97.1% measured using the double-π method. **c** The fidelity of the π pulse driven by the null-biased fiber-optic link is 97.8% measured using the double-π method. The half of the intercept of the exponential fitting curve represents the error rate of π pulse[45], as illustrated in the insets of (**b**, **c**). **d** The fidelity measured by the RB test for the coaxial cable link. The fidelity for the Clifford gate is 97.88% and the fidelity for the X_π gate is 98.92%. **e** The fidelity measured by the RB test for the null-biased fiber optic link. The fidelity for the Clifford gate is 98.35% and the fidelity for the X_π gate is 98.85%. The error bars in (**d**, **e**) represent the standard deviation.

vectors, the single-sideband mixing technique is employed[44]. The qubit state is initialized in the $\frac{1}{\sqrt{2}}(|0\rangle + \mathrm{i}|1\rangle)$ state by a calibrated $\pi/2$ pulse around the X (zero phase) axis. Then, by continuously varying the additional phase of the second pulse within the range of 0 to 2π and the pulse duration within the range of 0 to 100 ns, the two-dimensional Rabi oscillation data are obtained. In Fig. 7a, we plot the results using the polar coordinates defined by the phase difference of the two pulses and the duration of the second pulse. Note that in Fig. 7a the X, $-X$, Y, and $-Y$ axis of the Bloch sphere are marked by dashed lines, in correspondence to the positive and negative oscillations with the highest and zero contrast. It can be seen from the polar plot that owing to the frequency-doubling effect of the null-biased EOM, a phase variation of 2π of the AWG driving signal leads the qubit's rotation axis to rotate two cycles in the Bloch vector space. Based on such results, we conclude that complete vector control can be achieved using the null-biased fiber-optic link. For further results of the fidelity of single-qubit gates characterized by the double π metric and the randomized benchmarking (RB) metric, please refer to Supplementary Note 2, where it is demonstrated that both protocols yield similar results of π pulse fidelity, average Clifford gate fidelity and X_π gate fidelity. Note that in addition to the experiment of quasi-static phase modulation shown by Fig. 7a, it is also demonstrated that rapid, continuous modulation of the phase on the nanosecond time scale can be realized using the null-biased fiber-optic link. The details of this part are presented in Supplementary Note 3.

In Fig. 7b and c, we present the single qubit gate fidelity results measured by the double-π method[45]. The fidelity of a π pulse is determined to be 97.1% for the case of coaxial cable link and 97.8% for the case of null-biased fiber-optic link. In addition to the double-π method, the randomized benchmarking (RB) method[42,46] is also used in our work to measure the qubit fidelity, since it can separate errors in initial state preparation and final state readout from errors in gate operations. The results with the RB method are shown in Fig. 7d and e, from which the average gate fidelity of a π pulse is determined to be 97.88% for the coaxial cable link and 98.35% for the fiber-optic link, and the fidelity of the X_π gate is determined to be 98.92% for the coaxial cable link and 98.85% for the fiber-optic link. Based on the T_1 and T_{2E} results measured above, the theoretical coherence limit[47] of the gate fidelity is then determined to be 99% (see the detail in Supplementary Note 2). Summarizing the above measurements, we conclude that the fidelities of the single-qubit gate achieved using both driving methods are comparable.

We then demonstrate the parallelism of the null-biased fiber-optic link by showing that two qubits can be simultaneously controlled in the Bloch vector space. Using the circuit setup depicted in Fig. 8a, we first combine two microwave vector signals (2.556 GHz and 2.0725 GHz) with a combiner to serve as the modulation signal for the null-biased EOM. The two frequencies output by the photodetector in the cryogenic environment (5.112 GHz and 4.145 GHz) then resonantly drive two qubits (Q1 and Q2) via the transmission line. Finally, simultaneous readout is performed by driving two resonators (6.0409 GHz and 6.1093 GHz) through a coaxial cable. The results presented in Fig. 8b show simultaneous Rabi oscillations of the two qubits from the ground state. To conduct parallel vector rotation of the two qubits, the initial states are prepared with $X_{\frac{\pi}{2}}$ pulses. We then vary the axis angle (0, 12, 24… 168 degrees) of the second pulse of both frequencies to drive Rabi

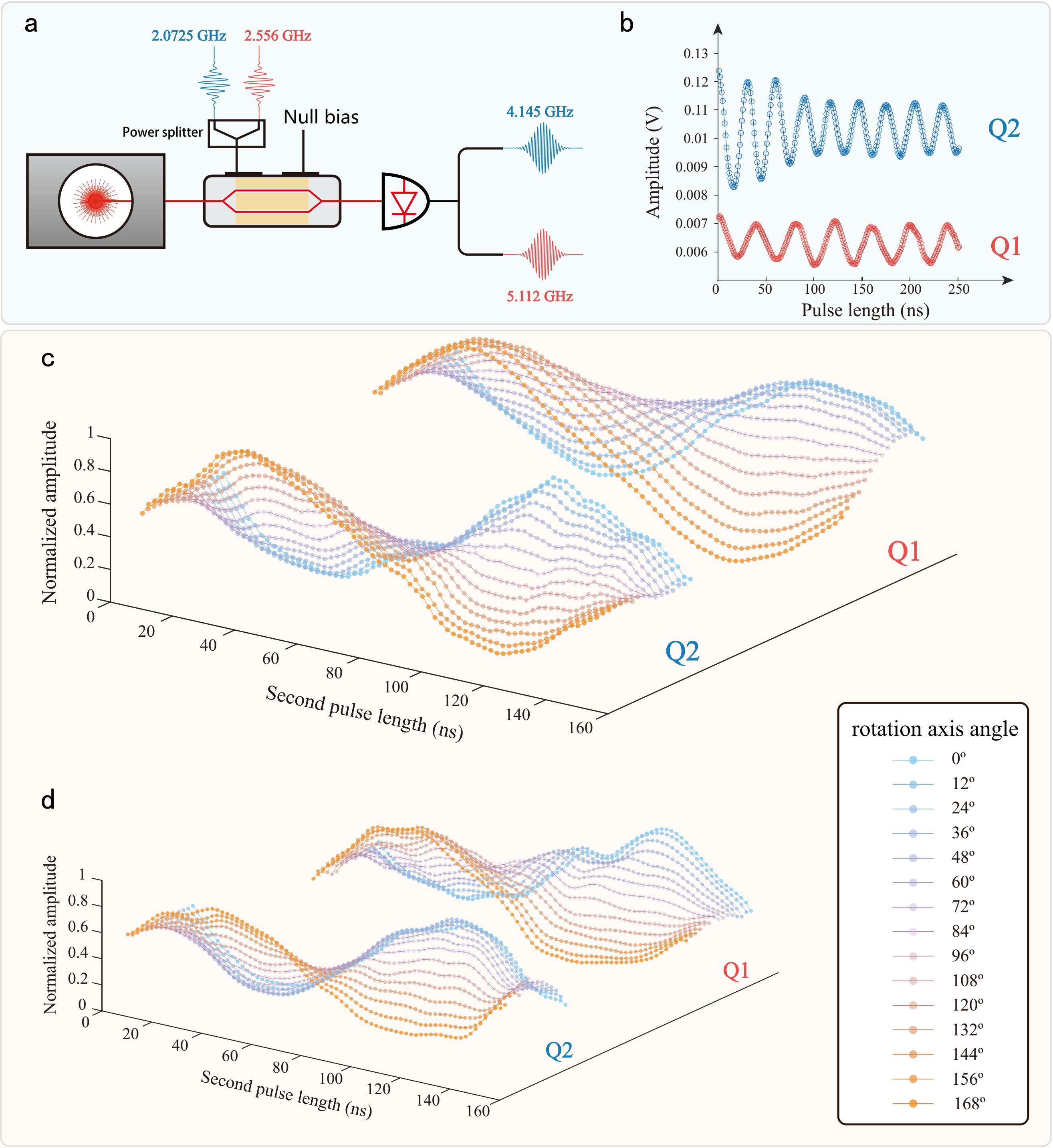

Fig. 8 | Simultaneous vector control of two qubits via the null-biased fiber-optic link. a The schematic diagram of measuring setup. Two combined vector microwave signals (2.556 GHz and 2.0725 GHz) serve as the modulation voltage signal of the EOM to drive the two qubits with qubit frequencies f_{01} = 5.112GHz and 4.145 GHz, respectively. **b** Simultaneous Rabi oscillations of the two qubits driven by the null-biased fiber-optic link. **c** Results of an experiment similar to that shown in Fig. 7. Here the rotation axes of the Bloch vectors of the two qubits are simultaneously adjusted to 0, 12, 24... 168 degrees. **d** Same results obtained using the coaxial cable link.

oscillations for a period. As shown in Fig. 8c, due to the presence of additional coupling between the two qubits and/or from other qubits of the sample which can't be tuned off thoroughly, slight offset is observed in the coherent oscillation center of Q1 when both qubits are driven simultaneously using the null-biased fiber-optic link. To confirm this point, a similar experiment is performed using the coaxial cable link and the result is presented in Fig. 8d for comparisons. As shown in Fig. 8d, such a phenomenon of slight offset can also be observed. Therefore, we conclude that there is no waveform distortion introduced by the fiber-optic link.

Discussion

In the following, we give a comparison of the quadrature- and null-biased fiber-optic links.

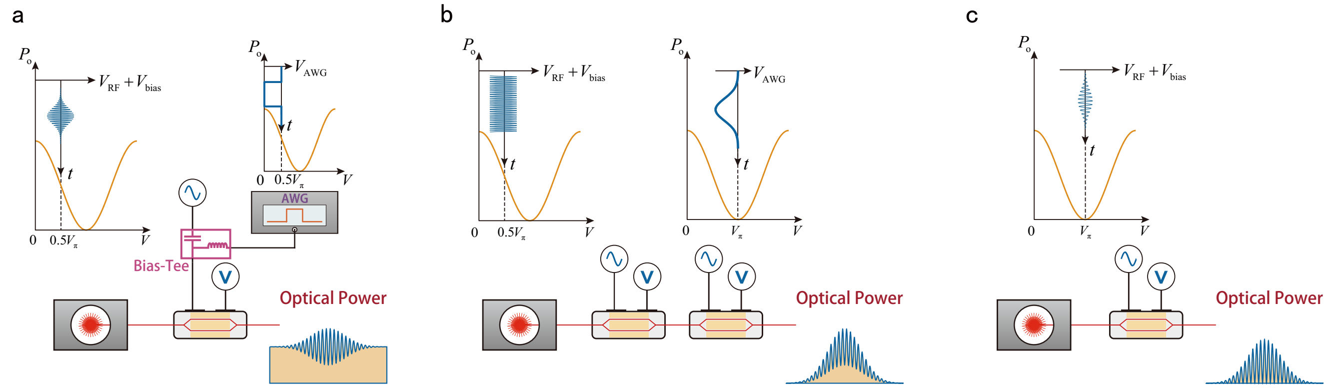

Fig. 9 | Schematics of different fiber-optic links. a Schematics of the fiber-optic link of Quad-1 with EOM biased at the quadrature point. **b** Schematics of the fiber-optic link of Quad-2 with EOM biased at the quadrature point. **c** Schematic of the fiber-optic link with EOM biased at the null point. Note that an extra square-wave pulse is required in the Quad-1, in order to cancel the optical power outside the signal window and in Quad-2, a second EOM is needed for envelope generation.

Fundamental difference

Previous work[35] has demonstrated the use of quadrature-biased EOMs for linear modulation of microwave signals[48]. In this context, considering continuous-wave modulations and using small signal approximations, the total output optical power from the EOM can be expressed as

$$\begin{aligned} P_{quad}(t) &= \frac{P_1}{2}\left[1-\sin\left(\pi\frac{V_m}{V_\pi}\sin\omega t\right)\right] \\ &\approx \frac{P_1}{2}(1-m_1\sin\omega t). \end{aligned} \tag{1}$$

Here P_1 represents the incident optical power into the EOM. V_π and $V_m\sin\omega t$ denote the EOM's half-wave voltage and the microwave signal applied to the EOM, respectively. $m_1=\pi V_m/V_\pi$ is the EOM's modulation depth.

On the other hand, in the proposed null-biased configuration and using small signal approximations, the output optical power of the null-biased EOM can be expressed as

$$\begin{aligned} P_{null}(t) &= \frac{P_2}{2}\left[1-\cos\left(\pi\frac{V_m}{V_\pi}\sin\omega t\right)\right] \\ &\approx \frac{P_2}{2}m_2^2(1-\cos 2\omega t) \end{aligned} \tag{2}$$

where P_2 denotes the EOM's incident optical power, and $m_2=\pi V_m/2V_\pi$ is the EOM's modulation depth.

A comparison of these two expressions for the output optical power reveals that, unlike the quadrature-biased case, the null-biased case inherently achieves full-depth modulation, i.e. the amplitude of the RF modulation being equal to that of the DC component, in regardless of the magnitude of the driving voltage V_m. Taking a typical assumption that the EOM's modulation depth is less than 1, it follows that the null-biased case produces less DC component (and hence less active heat and shot noise) when its generated RF signal equals that of the quadrature-biased case. Moreover, for a fixed strength of the RF signal, by increasing P_2, m_2 can be decreased. So because of the fundamental difference presented by Eqs. (1) and (2), the null-biased case can be operated in the small signal regime (i.e., small m_2) with less intra-band nonlinearity, while still keep the full-depth modulation condition being satisfied (i.e., $P_{null}(t)\sim 1-\cos 2\omega t$). We emphasize that such a feature of the null-biased case is not possible for the case of quadrature bias.

Complexity of experimental setup

There are two typical physical implementations for achieving linear pulse modulation of laser intensity using quadrature-biased EOMs as shown in Fig. 9a and b, which are referred as Quad-1 and Quad-2, respectively. Note that in the following discussion, the EOM's extinction ratio is assumed to be infinite.

As shown in Fig. 9a, Quad-1 employs a single quadrature-biased EOM. Assuming the driving signal is a Gaussian-shaped pulse given by $V_m\exp(-t^2/2\sigma^2)\sin\omega t$, the optical power output is expressed as $P^{(1)}_{quad}(t)=\frac{1}{2}P_1-\frac{1}{2}m_1P_1\exp(-t^2/2\sigma^2)\sin\omega t$. This output consists of a Gaussian-shaped signal component and a constant DC component equal to $\frac{1}{2}P_1$. To suppress the optical power outside the control pulse window, an additional square-wave pulse that dynamically changes the bias condition is then required, thus causing an extra burden of the involved waveform generator.

Figure 9 b illustrates the implementation of Quad-2, which requires two EOMs. The first EOM is biased at the quadrature point and performs linear continuous-wave modulation, producing an optical power output described by Eq. (1). The second EOM, which is biased at the null point, performs envelope modulation and energy cleaning outside the control pulse window. Assuming the second EOM is driven by a Gaussian-shaped pulse, the resulting optical power output is $P^{(2)}_{quad}(t)=\frac{1}{2}P_1\exp(-t^2/2\sigma^2)(1-m_1\sin\omega t)$. Note that here in contrast to Quad-1, both of the signal and DC components adopt Gaussian profiles with different amplitudes.

Figure 9 c shows the setup for our proposed null-biased scheme, where the null-biased EOM is driven by a Gaussian-shaped pulse of $V_m\exp(-t^2/2\sigma^2)\sin\omega t$. The optical power output, based on Eq. (2), is given by $P_{null}(t)=\frac{1}{2}m_2^2P_2\exp(-t^2/\sigma^2)(1-\cos 2\omega t)$. Different from Quad-2, both of the signal and DC components adopt Gaussian profiles, but with identical amplitudes. Since the DC component vanishes when the modulation is turned off, neither an extra square-wave pulse (which is required in Quad-1) nor a second EOM (which is required in Quad-2) is required to suppress the optical power outside the control pulse window.

Moreover, by matching the generated optical RF signal to that needed by the qubit, it can be observed that, for Quad-1 and Quad-2, the carrier frequency of the EOM modulation signal equals the qubit frequency. In contrast, for null-biased modulation, the carrier frequency of the EOM modulation signal is only half of the qubit frequency. It follows that the null-biased method imposes less stringent speed requirement on the involved RF instruments, which could potentially lower the building costs, especially for

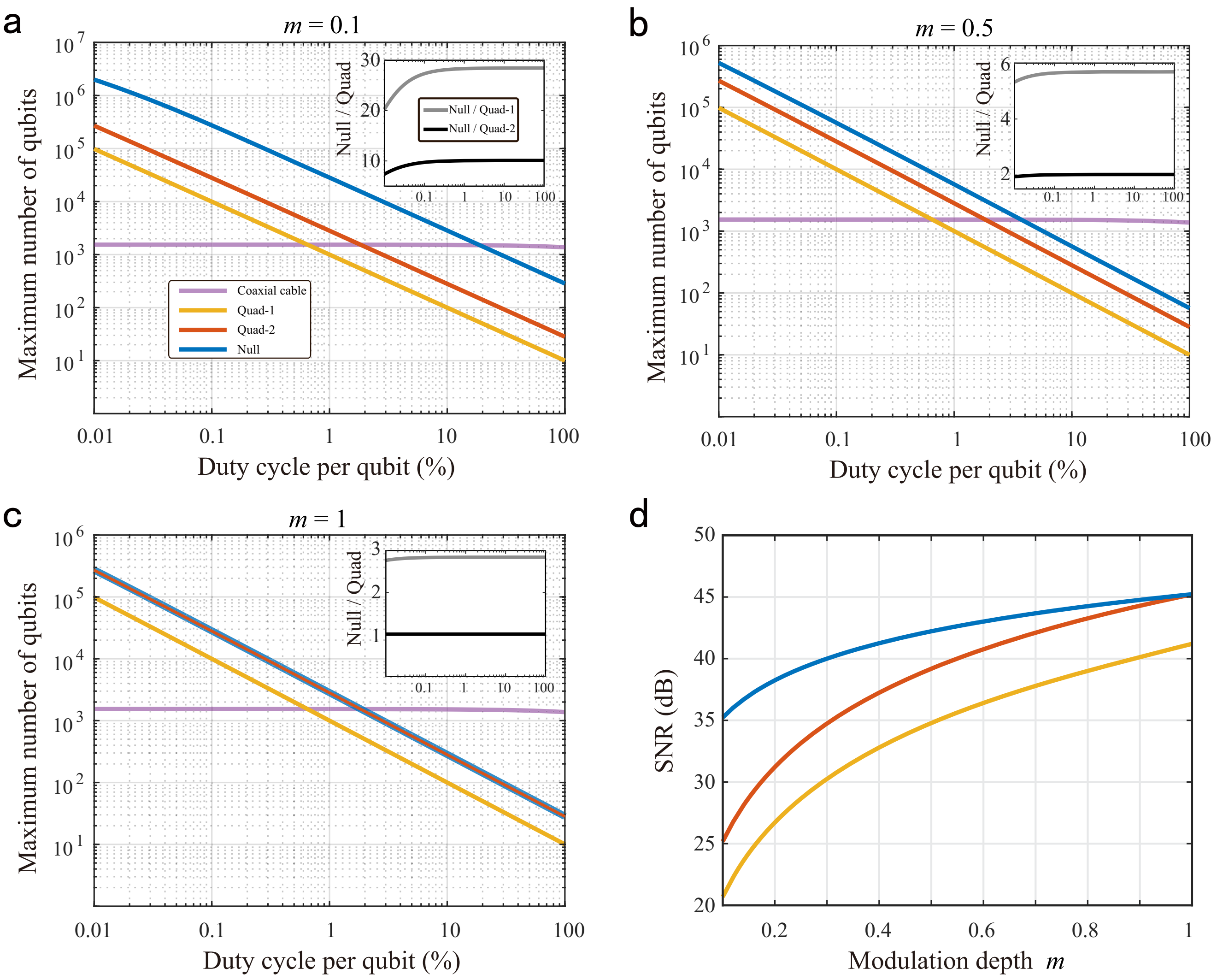

Fig. 10 | Maximum number of qubits that can be addressed simultaneously given the same cooling power. a For the optical modulation depth $m = 0.1$. **b** For the optical modulation depth $m = 0.5$. **c** For the optical modulation depth $m = 1$. The numerical results for Quad-1 (solid yellow line), Quad-2 (solid red line) and null-biased (solid blue line) fiber-optic links are presented. The result for coaxial cable link is depicted by the solid purple line. The inset shows the ratio of the maximum number of addressable qubits between the null-biased and two quadrature-biased cases. **d** The numerical results of SNR as a function of the optical modulation depth m for Quad-1, Quad-2 and null-biased fiber-optic links.

emerging qubit systems operating at frequencies in the tens of GHz range[8,49,50].

Maximum number of addressable qubits and SNR

We next analyze and compare the active heat load for the three cases illustrated by Fig. 9, based on which the maximum number of addressable qubits and SNR can be obtained. All parameters used in our simulation are selected to ensure that the envelope integrals of the RF components of the photocurrent are identical across all three cases. Moreover, the involved optical modulation depth m varies from 0 to 1, which covers beyond the small signal range discussed in Eqs. (1) and (2). Note that following the reference[35], here the optical modulation depth m is defined by $P_{out} = P_{ref}(1 + m\cos\omega t)$, where P_{out} and P_{ref} denote the output and reference power of the EOM, respectively.

Under the above condition, by comparing the DC component, i.e., the average photocurrent, the active heat loads for Quad-1, Quad-2, and null-biased fiber-optic link are calculated. Detailed numerical calculation are given in Supplementary Note 4. From the numerical calculations, the maximum number of addressable qubits is obtained, with results being presented in Fig. 10a–c as a function of the qubit control signal's duty cycle D, for optical modulation depth $m = 0.1, 0.5, 1$. It is evident that when the duty cycle is less than 1%, the fiber-optic links exhibit a significant advantage over the coaxial cable, although with the large duty cycle the contrary is the case. This agrees with the key conclusion drawn by the previous study[35]. As shown in the insets, when the modulation is less than full depth ($m < 1$), the null-biased fiber-optic link demonstrates a significantly higher number of addressable qubits over that of Quad-1 and Quad-2. This observation can be intuitively explained using the small signal analysis presented in Eqs. (1) and (2), which concludes that the null-biased case has a capability to produce equal amount of RF signal but less DC component.

Finally, we compare the SNR of the proposed null-biased fiber-optic link with that of the two quadrature-biased fiber-optic links. The primary noise seen by the qubits in the fiber-optic links is the shot noise of the photocurrent[35,51]. Intuitively, for the quadrature-biased cases of Quad-1 and Quad-2, since the DC component of the photocurrent is independent of the EOM's driving signal, the shot noise remains unchanged when the signal is reduced. In contrast, for the null-biased case, since the DC component of the photocurrent is quadratically proportional to the EOM's driving signal, the shot noise decreases when the signal is reduced. Therefore, the SNR for the quadrature-biased and null-biased cases should behave differently. To quantify the SNR, we use the following formula[35,51]

$$\mathrm{SNR} = 10\lg\left[\frac{\int_T \frac{1}{2} I_{sig}(t)^2 dt}{2e/T \int_T I_{dc} dt}\right]. \tag{3}$$

Here $I_{sig}(t)$ and I_{dc} denote the envelope of the in-band RF component and DC component of the photocurrent, respectively. e is the electron charge and $T = 3\tau$ (τ is the FWHM of the envelope) is the width of the gated signal window for integration[52–54]. Using the typical values of $P_1 = 4\,\mu W$, $P_2 \approx 100\,\mu W$, $T = 30\,ns$ and the photodiode responsivity $\eta = 0.5\,A/W$, and ensuring that the envelope integrals of the RF component of the photocurrent are the same across the three cases, SNRs for quadrature-biased cases Quad-1, Quad-2 and null-biased case as a function of the optical modulation depth m are calculated (see Supplementary Note 4 for details). From the results as shown in Fig. 10d, it can be seen that for m less than 1, the SNR of the null-biased case exhibits a significant advantage over that of the quadrature-biased cases Quad-1 and Quad-2.

We have proposed, demonstrated and investigated a null-biased fiber-optic link for coherent control of qubit systems. We have demonstrated a successful manipulation of the quantum state of a transmon qubit with a highest Rabi frequency over 100 MHz, which meets the need of fast quantum state operations. Through both frequency and time domain characterizations, we have concluded that the null-biased fiber-optic link does not affect the decoherence performance within the sensitivity limits posed by the coherence of the herein used qubit. We also have validated the effectiveness of the proposed method in vector controlling and parallel scalability. Compared to the two quadrature-biased cases, the proposed technique offers several advantages, including a reduced active heat load, improved SNR, and the relaxed requirement of experimental implementations. It is hoped that the proposed null-biased fiber-optic link can be a promising tool for the realization of large-scale superconducting quantum processor consisting of millions of qubits.

Methods

Components of the experimental setup

We utilize the Tektronix 5014C arbitrary waveform generator to produce intermediate frequency signals and predetermined Gaussian envelopes. These signals are combined with the vector microwave source R& S SGS100A for IQ mixing to generate vector signals for orthogonal control experiments on single qubit. A microwave source in pulse mode serves as the source for generating readout signals. Temporal control is achieved using the pulse delay generator DG645. Analog-to-digital conversion and data acquisition are conducted using the AlazarTech ATS9870 digital acquisition card. In the time-domain measurements, we employ the high-power readout method to achieve qubit state readout with high SNR[55,56]. The driving and probing fields are combined through a directional coupler placed with the chip at low temperature and transmitted to the sample via a short coaxial line. To generate the optical signal, we use a diode laser operating at a wavelength of 1550 nm and a commercial $LiNbO_3$ Mach-Zehnder intensity modulator at room temperature. The modulated optical signal is sent to a InGaAs photodiode, which is placed on top of the mixing chamber plate. In experiments where we simultaneously drive two qubits, we utilize the integrated system SHFQC by Zurich Instruments. We combine two SG channels into a single signal, which is used to drive the EOM. For readout of the qubit states, the QA channel simultaneously outputs readout pulses of two qubits, from which both phase and amplitude information of the two qubits are extracted.

Description of the circuit QED system

The qubit is driven indirectly through the resonator, which is coupled to the driving field. After applying the rotating wave approximation and setting the reduced Planck constant $\hbar = 1$, the complete Hamiltonian can be represented in the Schrödinger picture as follows[43,57,58]

$$\begin{aligned} H &= H_{JC} + H_D \\ &= \frac{1}{2}\omega_q\sigma_z + \omega_r a^\dagger a + g(\sigma_- a^\dagger + \sigma_+ a) + \epsilon(t)[a^\dagger e^{-i(\omega_d t + \phi)} + a e^{i(\omega_d t + \phi)}] \end{aligned} \tag{4}$$

where $\epsilon(t)$ is the amplitude of the qubit's driving field. In the dispersive regime where $g \ll |\Delta| = |\omega_q - \omega_r|$, the above Hamiltonian can be approximately diagonalized to second order of g/Δ by applying the transformation $U_{disp} = \exp[\frac{g}{\Delta}(\sigma_+ a - \sigma_- a^\dagger)]$[59]. The result is

$$\begin{aligned} H_{disp} &= U_{disp} H U_{disp}^\dagger \\ &\approx \omega_r a^\dagger a + \frac{1}{2}(\tilde{\omega}_q + 2\chi a^\dagger a)\sigma_z \\ &+ \frac{g\epsilon(t)}{\Delta}[\sigma_+ e^{-i(\omega_d t + \phi)} + \sigma_- e^{i(\omega_d t + \phi)}] + \epsilon(t)[a^\dagger e^{-i(\omega_d t + \phi)} + a e^{i(\omega_d t + \phi)}] \end{aligned} \tag{5}$$

where $\chi = g^2/\Delta$ is the longitudinal coupling strength. Transforming H_{disp} into the rotating frame by $U_{rot}(t) = \exp[\omega_d t(a^\dagger a + \frac{1}{2}\sigma_z)]$, we then have

$$\begin{aligned} H_{rot} &= U_{rot}(t) H_{disp} U_{rot}^\dagger(t) + i\dot{U}_{rot}(t) U_{rot}^\dagger(t) \\ &= \Delta_r a^\dagger a + \frac{1}{2}(\tilde{\omega}_q + 2\chi a^\dagger a - \omega_d)\sigma_z \\ &+ \frac{g\epsilon(t)}{\Delta}\left(\sigma_+ e^{-i\phi} + \sigma_- e^{i\phi}\right) + \epsilon(t)\left(a^\dagger e^{-i\phi} + a e^{i\phi}\right) \end{aligned} \tag{6}$$

where $\Delta_r = \omega_r - \omega_d$. Under the condition where the qubit is resonantly driven, i.e., $\omega_d = \tilde{\omega}_q + 2\langle a^\dagger a\rangle\chi$, the effect of the above Hamiltonian is to rotate the qubit around an axis on the equatorial plane of the Bloch sphere. The angle of the axis depends on the phase ϕ of the driving field and the rotation frequency or the Rabi frequency follows $\Omega_R \propto \epsilon(t)$[57].

Data availability

The data that support the findings of this study are available from the corresponding authors upon request.

Code availability

The codes of this study are available from the corresponding authors upon request.

References

1. Roushan, P. et al. Spectroscopic signatures of localization with interacting photons in superconducting qubits. *Science* **358**, 1175–1179 (2017).
2. Xu, K. et al. Emulating many-body localization with a superconducting quantum processor. *Phys. Rev. Lett.* **120**, 050507 (2018).
3. Yan, Z. et al. Strongly correlated quantum walks with a 12-qubit superconducting processor. *Science* **364**, 753–756 (2019).
4. Wu, Y. et al. Strong quantum computational advantage using a superconducting quantum processor. *Phys. Rev. Lett.* **127**, 180501 (2021).
5. Arute, F. et al. Quantum supremacy using a programmable superconducting processor. *Nature* **574**, 505–510 (2019).
6. Kwon, S., Tomonaga, A., Lakshmi Bhai, G., Devitt, S. J. & Tsai, J. S. Gate-based superconducting quantum computing. *J. Appl. Phys.* **129**, 041102 (2021).
7. Rasmussen, S. E. et al. Superconducting circuit companion—an introduction with worked examples. *PRX Quantum* **2**, 040204 (2021).

8. Siddiqi, I. Engineering high-coherence superconducting qubits. *Nat. Rev. Mater.* **6**, 875 (2021).
9. Koch, J. et al. Charge-insensitive qubit design derived from the Cooper pair box. *Phys. Rev. A* **76**, 042319 (2007).
10. Barends, R. et al. Coherent Josephson qubit suitable for scalable quantum integrated circuits. *Phys. Rev. Lett.* **111**, 080502 (2013).
11. You, J. Q., Hu, X., Ashhab, S. & Nori, F. Low-decoherence flux qubit. *Phys. Rev. B* **75**, 140515 (2007).
12. Yan, F. et al. The flux qubit revisited to enhance coherence and reproducibility. *Nat. Commun.* **7**, 12964 (2016).
13. Nguyen, L. B. et al. High-coherence fluxonium qubit. *Phys. Rev. X* **9**, 041041 (2019).
14. Place, A. P. M. et al. New material platform for superconducting transmon qubits with coherence times exceeding 0.3 milliseconds. *Nat. Commun.* **12**, 1779 (2021).
15. Zhang, H. et al. Universal fast-flux control of a coherent, low-frequency qubit. *Phys. Rev. X* **11**, 011010 (2021).
16. Gyenis, A. et al. Experimental realization of a protected superconducting circuit derived from the $0-\pi$ qubit. *PRX Quantum* **2**, 010339 (2021).
17. Roushan, P. et al. Chiral ground-state currents of interacting photons in a synthetic magnetic field. *Nat. Phys.* **13**, 146–151 (2017).
18. Yan, F. et al. Tunable coupling scheme for implementing high-fidelity two-qubit gates. *Phys. Rev. Appl.* **10**, 054062 (2018).
19. Strand, J. D. et al. First-order sideband transitions with flux-driven asymmetric transmon qubits. *Phys. Rev. B* **87**, 220505 (2013).
20. Caldwell, S. A. et al. Parametrically activated entangling gates using transmon qubits. *Phys. Rev. Appl.* **10**, 034050 (2018).
21. Google Quantum AI. Exponential suppression of bit or phase errors with cyclic error correction. *Nature* **595**, 383–387 (2021).
22. Gong, M. et al. Quantum walks on a programmable two-dimensional 62-qubit superconducting processor. *Nature* **372**, 948–952 (2021).
23. Fowler, A. G., Mariantoni, M., Martinis, J. M. & Cleland, A. N. Surface codes: towards practical large-scale quantum computation. *Phys. Rev. A* **86**, 032324 (2012).
24. Bharti, K. et al. Noisy intermediate-scale quantum algorithms. *Rev. Mod. Phys.* **94**, 015004 (2022).
25. Gidney, C. & Ekerå, M. How to factor 2048 bit RSA integers in 8 h using 20 million noisy qubits. *Quantum* **5**, 433 (2021).
26. Reiher, M., Wiebe, N., Svore, K. M., Wecker, D. & Troyer, M. Elucidating reaction mechanisms on quantum computers. *Proc. Natl Acad. Sci. USA* **114**, 7555–7560 (2017).
27. Babbush, R. et al. Encoding electronic spectra in quantum circuits with linear T complexity. *Phys. Rev. X* **8**, 041015 (2018).
28. Krinner, S. et al. Engineering cryogenic setups for 100-qubit scale superconducting circuit systems. *EPJ Quantum Technol.* **6**, 2 (2019).
29. Jin, X. et al. Thermal and residual excited-state population in a 3D transmon qubit. *Phys. Rev. Lett.* **114**, 240501 (2015).
30. Yan, F. et al. Distinguishing coherent and thermal photon noise in a circuit quantum electrodynamical system. *Phys. Rev. Lett.* **120**, 260504 (2018).
31. Huang, S. et al. Microwave package design for superconducting quantum processors. *PRX Quantum* **2**, 020306 (2021).
32. Yeh, J.-H., LeFebvre, J., Premaratne, S., Wellstood, F. C. & Palmer, B. S. Microwave attenuators for use with quantum devices below 100 mK. *J. Appl. Phys.* **121**, 224501 (2017).
33. Sinatkas, G., Christopoulos, T., Tsilipakos, O. & Kriezis, E. E. Electro-optic modulation in integrated photonics. *J. Appl. Phys.* **130**, 010901 (2021).
34. Davila-Rodriguez, J. et al. High-speed photodetection and microwave generation in a sub-100-mK environment. In *2019 Conf. Lasers and Electro-Optics (CLEO)* SF2N.1 (2019).
35. Lecocq, F. et al. Control and readout of a superconducting qubit using a photonic link. *Nature* **591**, 575–579 (2021).
36. Delaney, R. D. et al. Superconducting-qubit readout via low-backaction electro-optic transduction. *Nature* **606**, 489–493 (2022).
37. Devoret, M. H. & Schoelkopf, R. J. Superconducting circuits for quantum information: an outlook. *Science* **339**, 1169–1174 (2013).
38. Winzer, P. J., Neilson, D. T. & Chraplyvy, A. R. Fiber-optic transmission and networking: the previous 20 and the next 20 years. *Opt. Express* **26**, 24190–24239 (2018).
39. Arnold, G. et al. All-optical superconducting qubit readout. *Nat. Phys.* https://doi.org/10.1038/s41567-024-02741-4 (2025).
40. van Thiel, T.C. et al. Optical readout of a superconducting qubit using a piezo-optomechanical transducer. *Nat. Phys.* https://doi.org/10.1038/s41567-024-02742-3 (2025).
41. Warner, H. K. et al. Coherent control of a superconducting qubit using light. Preprint at https://arxiv.org/abs/2310.16155 (2023).
42. Barends, R. et al. Superconducting quantum circuits at the surface code threshold for fault tolerance. *Nature* **508**, 500–503 (2014).
43. Gambetta, J. M. et al. Qubit-photon interactions in a cavity: measurement-induced dephasing and number splitting. *Phys. Rev. A* **74**, 042318 (2006).
44. Naghiloo, M. Introduction to experimental quantum measurement with superconducting qubits. Preprint at https://arxiv.org/abs/1904.09291 (2019).
45. Chow, J. M. et al. Randomized benchmarking and process tomography for gate errors in a solid-state qubit. *Phys. Rev. Lett.* **102**, 090502 (2009).
46. Li, Z. et al. Error per single-qubit gate below 10^{-4} in a superconducting qubit. *npj Quant. Info.* **9**, 111 (2023).
47. Hyyppä, E. et al. Unimon qubit. *Nat. Commun.* **13**, 6895 (2022).
48. Cox III, C. H. Analog optical links: theory and practice. *Cambridge University Press* (2006).
49. Anferov, A., Harvey, S. P., Wan, F., Simon, J. & Schuster, D. I. Superconducting qubits above 20 GHz operating over 200 mK. *PRX Quantum* **5**, 030347 (2024).
50. Kjaergaard, M. et al. Superconducting qubits: current state of play. *Annu. Rev. Condens. Matter Phys.* **11**, 369–395 (2020).
51. Quinlan, F. et al. Exploiting shot noise correlations in the photodetection of ultrashort optical pulse trains. *Nat. Photon.* **7**, 290–293 (2013).
52. Bylander, J. et al. Noise spectroscopy through dynamical decoupling with a superconducting flux qubit. *Nat. Phys.* **7**, 565–570 (2011).
53. Steffen, M., Martinis, J. M. & Chuang, I. L. Accurate control of Josephson phase qubits. *Phys. Rev. B* **68**, 224518 (2003).
54. Boradjiev, I. I. & Vitanov, N. V. Control of qubits by shaped pulses of finite duration. *Phys. Rev. A* **88**, 013402 (2013).
55. Reed, M. D. et al. High-fidelity readout in circuit quantum electrodynamics using the jaynes-cummings nonlinearity. *Phys. Rev. Lett.* **105**, 173601 (2010).
56. Boissonneault, M., Gambetta, J. M. & Blais, A. Improved superconducting qubit readout by qubit-induced nonlinearities. *Phys. Rev. Lett.* **105**, 100504 (2010).
57. Blais, A. et al. Cavity quantum electrodynamics for superconducting electrical circuits: an architecture for quantum computation. *Phys. Rev. A* **69**, 062320 (2004).
58. Blais, A. et al. Quantum-information processing with circuit quantum electrodynamics. *Phys. Rev. A* **75**, 032329 (2007).
59. Blais, A., Grimsmo, A. L., Girvin, S. M. & Wallraff, A. Circuit quantum electrodynamics. *Rev. Mod. Phys.* **93**, 025005 (2021).

Acknowledgements

G.S. acknowledges the support by the Innovation Program for Quantum Science and Technology (No. 2021ZD0301701), the National Natural Science Foundation of China (No. 62288101), State Key Laboratory for Novel Software Technology at Nanjing University, Dengfeng Project of

Nanjing University, and Ministry of Education Engineering Research Center for Optoelectronic Materials and Chip Technology.

Author contributions

G.Z. and G.S. conceived and designed the experiment. W.X., K.Z., Z.L., Q.Z., G.Z. and G.S. built the experimental set-up. W.X., G.Z. and G.S. performed the experiment. W.X., C.C., G.Z., G.S. and P.W. analysed the data. T.G., T.Z., Y.S., L.J., H.M., M.Y., S.Z., B.L., S.Y., Y.Y., J. Zhang and J. Zhu fabricated the samples. All authors contributed to the manuscript.

Competing interests

The authors declare no competing interests.

Additional information

Supplementary information The online version contains supplementary material available at https://doi.org/10.1038/s41467-025-57820-8.

Correspondence and requests for materials should be addressed to Guanghao Zhu or Guozhu Sun.

Peer review information *Nature Communications* thanks Florent Lecocq, and the other, anonymous, reviewers for their contribution to the peer review of this work. A peer review file is available.

Reprints and permissions information is available at http://www.nature.com/reprints